# Electrode segmentation in reverse electrodialysis: Improved power and energy efficiency

Catarina Simões[a,b,1], Diego Pintossi[a,c,1], Michel Saakes[a], Zandrie Borneman[c,d], Wim Brilman[b], Kitty Nijmeijer[c,d,*]

[a] Wetsus, European Centre of Excellence for Sustainable Water Technology, Oostergoweg 9, 8911 MA Leeuwarden, the Netherlands
[b] Sustainable Process Technology, Faculty of Science and Technology, University of Twente, P.O. Box 217, 7500 AE Enschede, the Netherlands
[c] Membrane Materials and Processes, Department of Chemical Engineering and Chemistry, Eindhoven University of Technology, P.O. Box 513, 5600 MB Eindhoven, the Netherlands
[d] Dutch Institute for Fundamental Energy Research (DIFFER), P.O. Box 6336, 5600 HH Eindhoven, the Netherlands

## GRAPHICAL ABSTRACT
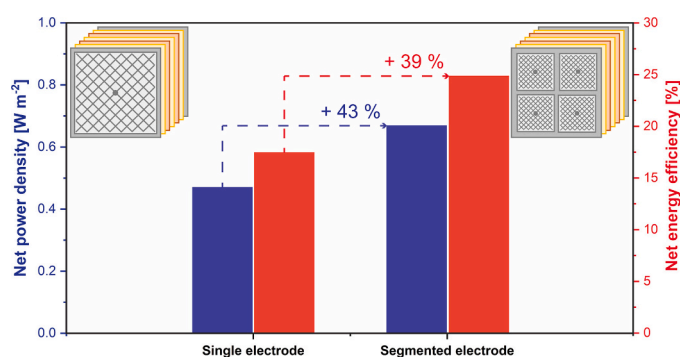


## ARTICLE INFO

## ABSTRACT

Reverse electrodialysis harvests energy from salinity gradients establishing a renewable energy source. High energy efficiencies are fundamental to up-scale the process and to minimize feedwater pre-treatment and pumping costs. The present work investigates electrode segmentation to strategically optimize the output power density and energy efficiency. Electrode segmentation allows the current density to be tuned per electrode segment. Segmentation experiments were performed with a dedicated electrode configuration in a cross-flow stack using a wide range of residence times. Moreover, an experimentally validated model was extended and used to further compare single and segmented electrode configurations. While operating the electrode segments, the highest efficiencies were obtained when considering the overall power, i.e. not maximized by segment. Results show that at a given net power density ($0.92\,\mathrm{W\cdot m^{-2}}$), electrode segmentation increases the net energy efficiency from 17% to 25%, which is a relative increase of 43%. Plus, at 40% net energy efficiency the net power output for a segmented electrode configuration ($0.67\,\mathrm{W\cdot m^{-2}}$) is 39% higher than in a single electrode configuration. Higher power density reduces capital investment and higher energy efficiency reduces operating costs. Electrode segmentation increases these parameters compared to a single electrode and can be potentially applied for up-scaling.

* Corresponding author at: Membrane Materials and Processes, Eindhoven University of Technology, P.O. Box 513, 5600 MB Eindhoven, the Netherlands.
  E-mail address: d.c.nijmeijer@tue.nl (K. Nijmeijer).
  [1] Equally contributed to the manuscript.

## 1. Introduction

Given the growing global energy demand, there is a great societal need for clean and renewable energy sources to replace the use of polluting fossil fuels and reduce $CO_2$ emissions [1]. One promising source of renewable energy is salinity gradient (also known as blue energy) where the energy results from the reversible mixing of two streams with different salinities. The salinity gradient is widely available anywhere a river runs into the sea, being a non-intermittent renewable energy source, opposite to solar and wind energy [2]. The theoretical energy that can be generated from mixing 1 m$^3$ of river water (1 g NaCl·L$^{-1}$) with 1 m$^3$ of seawater (30 g NaCl·L$^{-1}$) is 1.7 MJ [3]. Worldwide the technical potential for salinity gradient energy was estimated at 983 GW [4]. With its implementation, energy-related emissions could be reduced by 25%, 27%, and 8% of $CO_2$, $CH_4$, and $N_2O$, respectively [4].

One main technology to harvest salinity gradient energy is reverse electrodialysis (RED) [5]. The RED process consists of a stack with an alternating series of cation (CEM) and anion (AEM) exchange membranes (Fig. 1). Compartments are established with spacers between the membranes, where seawater and river water flow alternately alongside the membrane. Since ion exchange membranes (IEMs) have selectivity either towards cations (CEMs) or anions (AEMs), a Donnan potential is generated across the membranes. One cell pair comprises of one AEM, one CEM, one river compartment, and one seawater compartment. When multiple cell pairs are stacked, this potential is accumulated. The potential difference over the membranes drives the transport of ions through the membranes from the seawater towards the river water compartment. Finally, enclosing the membrane pile, an electrode is placed at each end of the stack. A redox solution is recirculated to convert the ionic current into an electrical current, which powers an external load [6].

In the past years, several studies were conducted to improve the process' power density as well as its efficiency. This includes membrane modification, such as monovalent-ion-selective membranes, surface modifications and profiled membranes [7–10], fouling prevention and monitoring [11–15], spacer thickness effect or no spacer present by using corrugated membranes [16,17], flow velocity of the feedwaters [18], scalability of the cross-flow stack [19], prevention of ionic shortcut currents [20], modelling of the RED process with different flow strategies (co-flow, counter-flow and cross-flow) and model optimization of the RED process [21–24]. Furthermore, the potential for large scale application has been proven with pilot plants [25,26].

To establish RED as a commercial technology, it is crucial to use large scale stacks with sufficient energy efficiency [27]. With more ion exchange, to allow sufficient energy efficiency, the salt concentration in the river water increases significantly along the length of the stack, resulting in a drastic decrease of the local ohmic electrical resistance and a drop of electromotive force inside the stack along the flow path length. This leads to a non-homogeneous current distribution over the length of the active membrane area [22]. When using a stack with a single pair of electrodes, i.e. one anode and one cathode, only one external load can be set to harvest the energy. While this single load can be tuned for maximum power production, this represents a compromise between the optimal loads of different sections of the active area [28].

For a given stack size, the required pumping energy is reduced at longer residence times due to a lower flow velocity [19]. Moreover, feedwaters need to be pre-treated to avoid fouling inside the RED stacks [29]. The extraction of more energy per m$^3$ of seawater and river water compensates the energy consumption associated with pumping and pretreatment of the feedwaters. In brief, the operation of stacks to achieve sufficient energy efficiency introduces new challenges that limit the

maximum RED power output [30].

A promising strategy to increase energy efficiency without incurring additional power output losses is electrode segmentation. Segmentation has been used before to map the current density inside electrochemical cells, such as proton-exchange membrane fuel cell [31,32] or redox flow batteries [33,34], and for process optimization in electrodialysis [35,36]. In RED, segmentation allows the optimization of the performance by tuning the resistive load per segment. In this way, the external load can be adjusted to the local electrode segment electrical resistance. Such adjustment enables a higher power density output and energy efficiency. Veerman et al. [28] made the first experimental study of segmentation in RED with a scaled-up stack (active area of 25 cm × 75 cm). Segmentation was studied using three-electrode segments (25 cm × 25 cm, each). The stack was operated horizontally with a co-flow feed configuration. The optimal resistance was found for each electrode segment and the corresponding current was extracted. This resulted in a power density increase of 11%, from 0.44 to 0.49 W·m$^{-2}$, when compared with the same stack with the three-electrode segments connected as one electrode. The same author published a model regarding electrode segmentation [21], which proved an increase of power by about 15% when using an infinite number of segments. In this model, the non-ideal behaviour of membranes was accounted for and the stack (10 cm × 10 cm) was operated with a co-flow feed configuration. Besides infinite segmentation, the model also predicted the effect of 2 to 5 electrode segments, with a power increase between 13 and 17%, respectively. While surprising, the higher increase for a limited number of segments rather than for an infinite number of electrode segments can be explained by the trade-off between high power in the first stages and the need to preserve gradient for the last segments. More recently, Vermaas et al. [22] modelled a RED stack to study the influence of the feed flow configuration, the seawater fraction and the
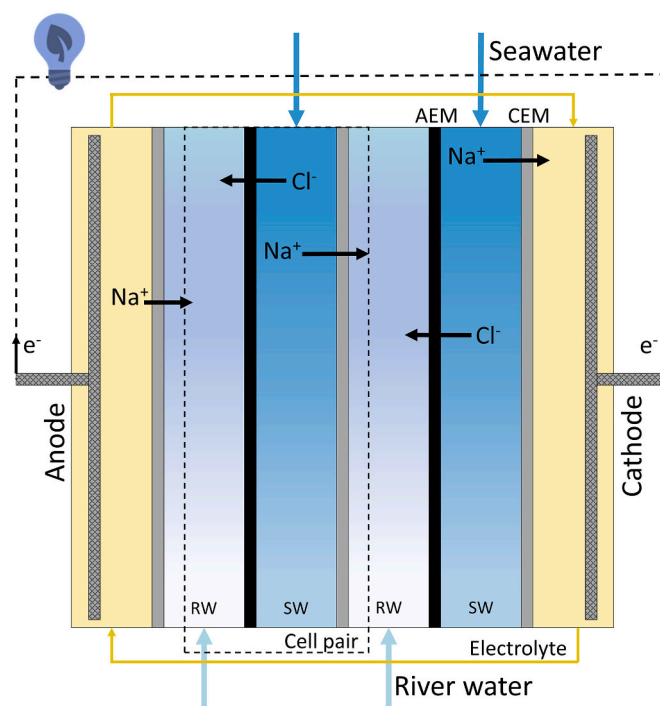


**Fig. 1.** Working principle of RED. Two cell pairs are present in the scheme plus an extra CEM to shield the feedwater from the electrode rinse solution. One cell pair is composed of one AEM, one CEM, river compartment and seawater compartment. In a RED stack, multiple cell pairs are placed between the electrodes.

electrode segmentation on the energy efficiency. The model of Vermaas et al. assumed ideal IEMs, no concentration polarization effects and considered a fixed residence time for river water. The results showed that for all configurations higher efficiencies were achieved when the electrode was segmented. The energy efficiency increases by approximately 15% for the same ratio of seawater and river water when using two electrode segments compared to a single electrode.

The present research aims to investigate experimentally and by modelling the behaviour of electrode segmentation in a RED cross-flow stack. This includes the integration of previous modelling works [21,22] into a new dedicated model, able to characterize the cross-flow stack either with a single electrode or different electrode segments. Furthermore, besides studying the interaction between electrode segments, the overall maximum power density of the electrode segments was optimized.

## 2. Materials and methods

### 2.1. RED modelling

To model the RED stack with segmented electrodes in a cross-flow configuration, two models presented in the literature were combined: the model proposed by Veerman et al. [21] and the model by Vermaas et al. [22]. Veerman's model includes membrane properties, osmosis and salt transport, but it is limited to co-flow and counter-flow configurations, while Vermaas' model includes the cross-flow configuration, but it only considers ideal membranes (having zero electrical resistance and perfect permselectivity).

The models were combined and used as reported with the addition of segmentation along the seawater direction to simulate a 2 by 2 segmented electrode configuration. Fig. S1a describes the segmented cross-flow stack, while Fig. 2 depicts the discretization scheme.

The modified Nernst equation expresses the electromotive force (V) available at each point in the grid:

$$E_{i,j} = (\alpha_{AEM} + \alpha_{CEM})\frac{RT}{zF} ln\left(\frac{\gamma_{i,j}^{SW} C_{i,j}^{SW}}{\gamma_{i,j}^{RW} C_{i,j}^{RW}}\right) \tag{1}$$

where $\alpha$ is the permselectivity of AEM and CEM ($-$), $R$ is the universal gas constant (J·mol$^{-1}$·K$^{-1}$), $T$ is the absolute temperature (K), $z$ is the

ion valence ($-$), $F$ is the Faraday constant (C·mol$^{-1}$), $\gamma$ is the molar activity coefficient ($-$) estimated with the TCPC model of Ge et al. (a semi-empirical model combining Pitzer long-range interactions and short-range solvation effect) [37], and $C$ is the salt concentration (mol·m$^{-3}$).

The area resistance ($\Omega$·m$^2$) of the cell was given by:

$$R_{i,j}^{cell\ pair} = R_{AEM} + R_{CEM} + \frac{1}{f}\frac{d_{RW}}{\kappa_{i,j}^{RW}} + \frac{1}{f}\frac{d_{SW}}{\kappa_{i,j}^{SW}} + \frac{R_{blank}}{N_{CP}} \tag{2}$$

$$\kappa = \Lambda \cdot C \tag{3}$$

where $R_{AEM}$ and $R_{CEM}$ are the area electrical resistance of the AEM and CEM ($\Omega$·m$^2$), respectively, $f$ is the spacer shadow factor ($-$), a fitting parameter accounting for the presence of non-conductive spacers in the water compartments, $d$ is the water compartment thickness (m), $\kappa$ is the conductivity of feedwaters (S·m$^{-1}$), $R_{blank}$ is the area electrical resistance of the shielding CEMs and electrodes ($\Omega$·m$^2$), $N_{CP}$ is the number of cell pairs ($-$), and $\Lambda$ is the molar conductivity of NaCl (S·m$^{-1}$·mol$^{-1}$).

To implement electrode segmentation in the model, the four load voltages ($U_{S1}$, $U_{S2}$, $U_{S3}$, and $U_{S4}$) were used for the four segments (S1, S2, S3, and S4 in Fig. 2). The load voltages (V) applied to the segments were:

$$U_{i,j}^{load} = U_{S1} \ for \ 0 \le i < \frac{N}{2}, \ 0 \le j < \frac{N}{2}$$

$$U_{i,j}^{load} = U_{S2} \ for \ 0 \le i < \frac{N}{2}, \ \frac{N}{2} \le j \le N$$

$$U_{i,j}^{load} = U_{S3} \ for \ \frac{N}{2} \le i \le N, \ 0 \le j < \frac{N}{2}$$

$$U_{i,j}^{load} = U_{S4} \ for \ \frac{N}{2} \le i \le N, \ \frac{N}{2} \le j \le N$$

When the loads were applied to the segments, the current density (A·m$^2$) at all points was:

$$J_{i,j} = \frac{E_{i,j} - U_{i,j}^{load}}{R_{i,j}^{cell}} \tag{4}$$

The salt flux (mol·m$^{-2}$·s$^{-1}$) at each point of the discretization grid was expressed as the sum of current transport and co-ion transport
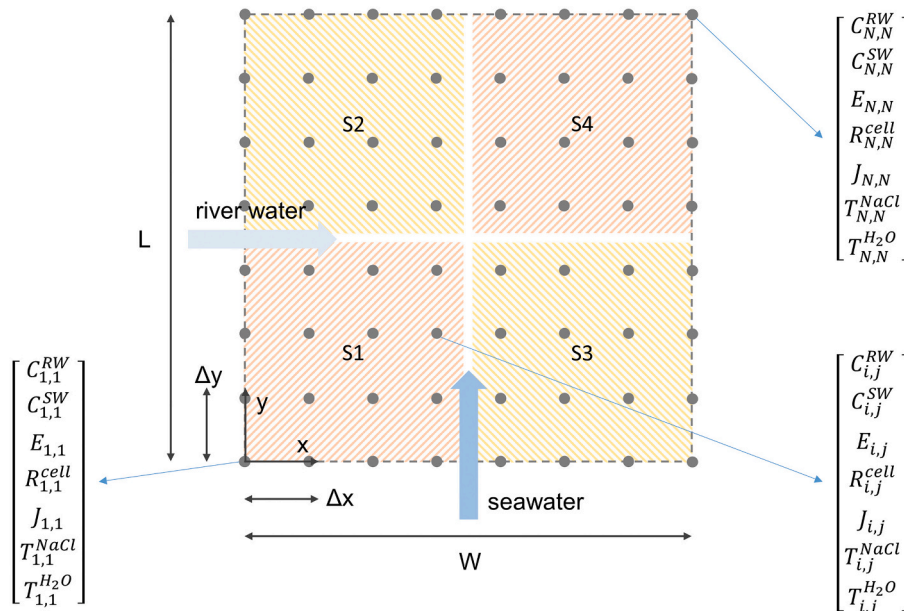


**Fig. 2.** Scheme of the discretization strategy adopted in the RED model. The cell pair is reduced to a matrix where to each point a set of properties relative to the feedwaters and membranes is associated.

through the AEM and CEM:

$$T_{i,j}^{NaCl} = \frac{J_{i,j}}{F} + 2(C_{i,j}^{SW} - C_{i,j}^{RW})\frac{D_{NaCl}}{l_m} \qquad (5)$$

where $D_{NaCl}$ is the average diffusion coefficient of NaCl through the AEM and CEM (m$^2$·s$^{-1}$), $l_m$ is the membrane thickness (m), and factor 2 is introduced to account for the diffusion through both membrane types.

The volumetric flux of water through the membranes (m·s$^{-1}$) was given by [21]:

$$T_{i,j}^{H_2O} = -2(C_{i,j}^{SW} - C_{i,j}^{RW})\frac{D_{H_2O}}{l_m}\frac{MW_{H_2O}}{\rho_{H_2O}} \qquad (6)$$

where $D_{H_2O}$ is the average diffusion coefficient of water through the AEM and CEM (m$^2$·s$^{-1}$), the factor 2 was introduced to account for the diffusion through both membrane types, $MW_{H_2O}$ is the molecular weight of water (kg·mol$^{-1}$), and $\rho_{H_2O}$ is the density of water (kg·m$^{-3}$).

The change in concentration in the active area can be described by the sum of the salt transport due to migration and diffusion (co-ions), plus water transport, as in the following partial differential equations (PDEs):

$$\frac{\partial C_{i,j}^{SW}}{\partial y} = -\frac{\Delta x}{\Delta\phi_{SW}}T_{i,j}^{NaCl} + C_{i,j}^{SW}\frac{\Delta x}{\Delta\phi_{SW}}T_{i,j}^{H_2O} = -\frac{W}{\phi_{SW}}T_{i,j}^{NaCl} + C_{i,j}^{SW}\frac{W}{\phi_{SW}}T_{i,j}^{H_2O} \qquad (7)$$

$$\frac{\partial C_{i,j}^{RW}}{\partial x} = +\frac{\Delta y}{\Delta\phi_{RW}}T_{i,j}^{NaCl} - C_{i,j}^{RW}\frac{\Delta y}{\Delta\phi_{RW}}T_{i,j}^{H_2O}$$
$$= +\frac{L}{\phi_{RW}}T_{i,j}^{NaCl} - C_{i,j}^{RW}\frac{L}{\phi_{RW}}T_{i,j}^{H_2O} \qquad (8)$$

where $\Delta x$ and $\Delta y$ are the discretization intervals (m), $\phi$ is the feed flow rate (m$^3$·s$^{-1}$), $\Delta\phi$ is the feed flow rate in $\Delta x$ or $\Delta y$ (m$^3$·s$^{-1}$), $L$ is the length of the active area (m), and $W$ is its width (m). The two governing PDEs are solved numerically using the Forward Euler method (Eqs. (9) and (10)), thus obtaining the matrix of the concentrations at steady state.

$$C_{i+1,j}^{SW} = C_{i,j}^{SW} + dy\left(-\frac{W}{\phi_{SW}}T_{i,j}^{NaCl} + C_{i,j}^{SW}\frac{W}{\phi_{SW}}T_{i,j}^{H_2O}\right) \qquad (9)$$

$$C_{i,j+1}^{RW} = C_{i,j}^{RW} + dx\left(+\frac{L}{\phi_{RW}}T_{i,j}^{NaCl} - C_{i,j}^{RW}\frac{L}{\phi_{RW}}T_{i,j}^{H_2O}\right) \qquad (10)$$

From the solution concentrations, the electromotive force, cell resistance, current density, power (and power density), and efficiencies were calculated. Custom Python 3.6 scripts and functions were developed for this purpose. The grid size was $500 \times 500$ points. Further grid refinement did not significantly affect the model results, while it increased the computation time.

The total power output was maximized by varying the ohmic loads applied to the four segments using a SLSQP (sequential least squares programming) algorithm. The scypy.optimize.minimize function was
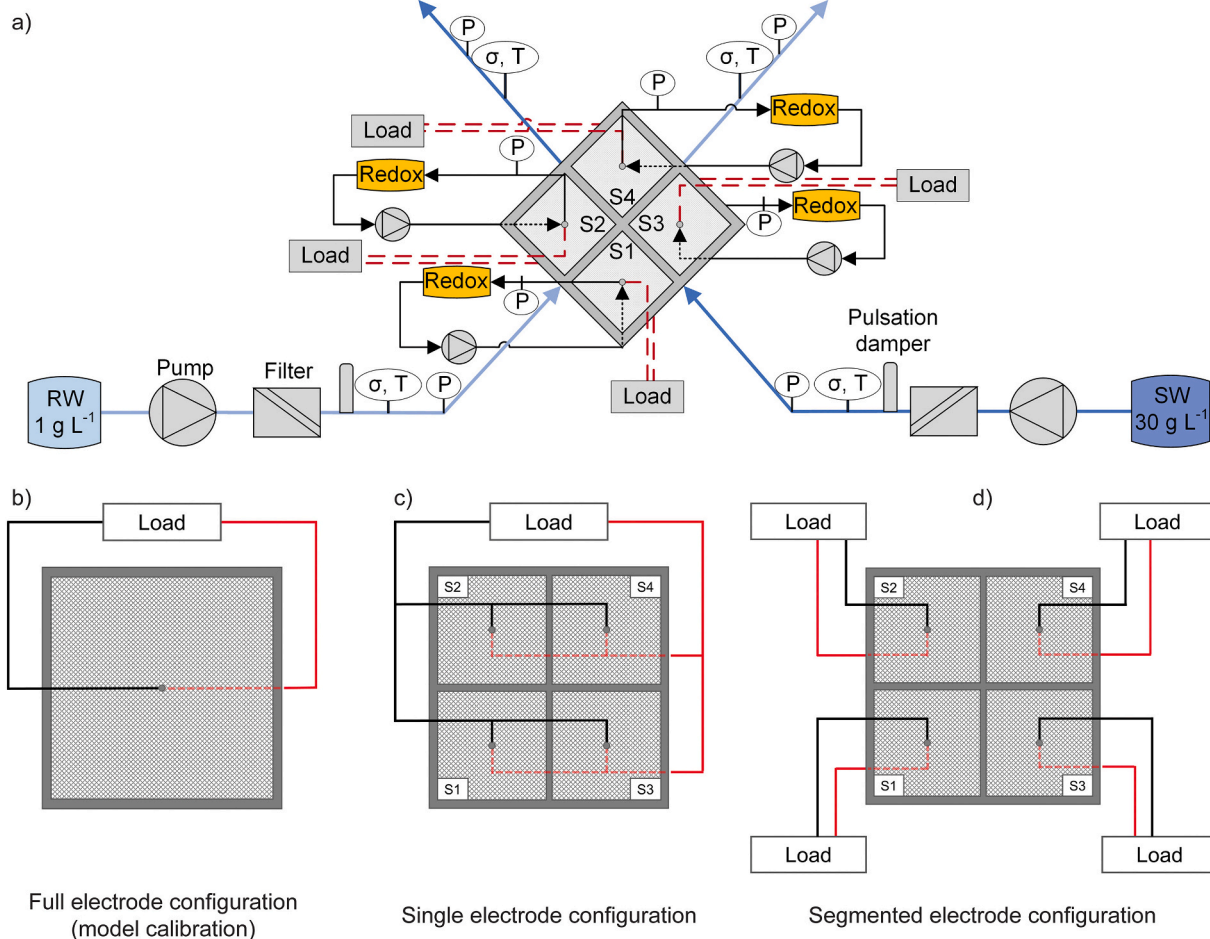


**Fig. 3.** a) Flow diagram for the operation of the segmented electrode stack configuration. b) Electrode and external load representation of the stack with a 22 cm × 22 cm electrode (full electrode configuration). c) Electrode and external load representation of the stack with four 10 cm × 10 cm electrode segments connected to a single external load (single electrode configuration). d) Electrode and external load representation of the stack with four 10 cm × 10 cm electrode segments connected to four separate external ohmic loads (segmented electrode configuration).

used for this purpose ($-P_{gross}$ was the minimized function).

Table S1 summarizes all the model input parameters used in the present work and how they were evaluated.

For both model and experimental data, the gross power produced by the stack was given by:

$$P_{gross} = U_{load} I \tag{11}$$

where $U_{load}$ is the voltage drop measured if a load is applied to the stack (V) and $I$ is the current extracted from the stack (A).

To calculate the efficiency of the stack operation, the total Gibbs energy available in the salinity gradient (J), was considered:

$$\Delta G = T \cdot \Delta S = T \cdot (S_{mix} - S_{SW} - S_{RW}) \tag{12}$$

$$S = -R n_{TOT} \sum_i x_i \ln(\gamma_i x_i) \text{ with } i = Na^+, Cl^-, H_2O \tag{13}$$

where $S$ is the entropy ($J \cdot K^{-1}$), $n_{TOT}$ is the total number of moles (mol), $x_i$ is the fraction of element $i$ ($-$).

Considering in Eq. (13) the flow rates of the feedwaters ($m^3 \cdot s^{-1}$) rather than the compartment volumes ($m^3$), $n_{TOT}$ becomes the number of moles per second ($mol \cdot s^{-1}$). The entropy was calculated per unit of time ($W \cdot K^{-1}$), and Eq. (12) expressed the available power (W), which can be directly compared to the stack power output to calculate the energy efficiency.

The (gross) energy efficiency (%) considered the gross power produced compared to the total available Gibbs energy at the inlet (complete mixing was assumed):

$$\eta_{energy} = 100 \frac{P_{gross}}{\Delta G_{in}} \tag{14}$$

The pumping losses (W) were calculated as the energy consumed to pump the seawater and the river water respectively [21]:

$$P_{pump} = \phi_{SW} dP_{SW} + \phi_{RW} dP_{RW} \tag{15}$$

$$dP_{RW} = K \frac{W \phi_{RW}}{L d_{RW}{}^3} \tag{16}$$

$$dP_{SW} = K \frac{L \phi_{SW}}{W d_{SW}{}^3} \tag{17}$$

where $dP$ is the pressure drop between feedwater inlet and outlet (Pa), $K$ is the fitting coefficient ($Pa \cdot s$) used to describe the pumping energy, and $\phi$ is the flow rate of the feedwater ($m^3 \cdot s^{-1}$).

By subtracting the pumping losses from the gross power, the net power (W) was obtained:

$$P_{net} = P_{gross} - P_{pump} \tag{18}$$

From the net power, the net energy efficiency (%) was determined:

$$\eta_{net} = 100 \frac{P_{net}}{\Delta G_{in}} \tag{19}$$

All power figures were converted to power densities by dividing the power values by the total membrane area ($A_{total} = 2W \cdot L \cdot N_{CP}$, accounting for the area of CEMs and AEMs in all cell pairs).

$$P_d = \frac{P}{2W \cdot L \cdot N_{CP}} \tag{20}$$

### 2.2. Stack configuration & electrodes

A cross-flow reverse electrodialysis stack (REDstack BV, the Netherlands) was used to investigate the effect of electrode segmentation on performance. The stack design details can be found in previous research [16,29,38]. The stack, with 22 cm × 22 cm active membrane area, contained 10 cell pairs (0.968 $m^2$ of total active membrane area). The number of cell pairs was chosen according to the desired experiment duration and volume of the feedwater reservoirs (at the highest flow rate, water consumption is approximately 2.5 L·h$^{-1}$ per cell pair).

Each cell pair consisted of one Fujifilm type 10 CEM and one Fujifilm type 10 AEM (FUJIFILM Manufacturing Europe BV, the Netherlands). The properties of these membranes are reported by Moreno et al. [19]. To close the electrode compartments, two CEMs are placed at each end, for double-shielding purpose, adding a total of three extra Fujifilm type 10 CEMs, instead of one extra CEM. The membranes were separated by 155 μm thick woven net-spacers (Deukum GmbH, Germany), with netting Saatifil PES 153/55 (Saati SpA, Italy). For the model validation, standard 22 cm × 22 cm (Fig. 3b) Ti-mesh 1.0 electrodes with 2.5 μm Pt galvanic coating were used as anode and cathode (MAGNETO Special Anodes BV, the Netherlands).

For segmentation, a dedicated electrode configuration was manufactured (REDstack BV, the Netherlands) with four 10 cm × 10 cm electrodes placed at the endplates with 1.5 cm distance between each other (Figs. 3d, S1b), while the total active membrane area was kept at 0.968 $m^2$. The electrodes were made of Ti-mesh with a Ru/Ir mixed metal oxide coating for anode and cathode (MAGNETO Special Anodes BV, the Netherlands). As electrode rinse solution a mixture of 0.2 M K$_4$Fe(CN)$_6$, 0.2 M K$_3$Fe(CN)$_6$ and 0.15 M NaCl was used (96%, 96% and 100% purity, respectively, VWR Chemicals, Belgium). Due to the special electrode configuration, the electrode rinse solution was pumped independently into each electrode compartment (Fig. S1b) at a flow rate of 150 mL·min$^{-1}$ using a peristaltic pump (Cole-Palmer, Masterflex L/S Digital drive, USA) with two double pump heads to avoid pulsations (Cole-Palmer, Masterflex L/S Two-Channel Easy-Load II, USA). Fig. 3a provides a schematic illustration of the feed water directions, electrical connections and sensors during the segmented electrode stack operation.

### 2.3. Feedwaters and sensors

Artificial feedwaters were made of 30 g NaCl·L$^{-1}$ and 1 g NaCl·L$^{-1}$ (99.9% purity, Regenit, Esco, the Netherlands), for seawater and river water, respectively. The two solutions were pumped at the same flow velocity using diaphragm pumps (Grundfos DDA220, Denmark). Pulsation dampers (PDS250 PVC/FKM, Prominent GmbH, Germany) were placed between the pumps and the stack to mitigate the pump pulsation. Also, cartridge filters with 1 μm pore size (Filter Technics, Belgium) were placed before the stack (Fig. 3a). Outlet flow velocities were measured gravimetrically. Conductivity and temperature were measured in-line (VStar22, Thermo Fisher Scientific, USA) at the inflow and outflow of each stream. The inlet temperatures were set to 25 °C. The absolute pressure was measured with calibrated sensors (MIDAS SW, JUMO GmbH, Germany) in the same points as the conductivity and at the electrode rinse solutions. The data were collected with a data logger (Memograph M, Endress + Hauser, Germany). Salt concentrations were calculated from conductivity values based on an experimental calibration curve (Fig. S2). The hydrodynamic losses were determined as the product of the differential pressure across the stack and the flow rate (Eq. (15)) [28].

### 2.4. Experimental procedure

#### 2.4.1. Experiments for model validation with standard stack

To identify the spacer shadow factor and the average salt diffusion coefficient values through the membranes, a separate experiment with full electrode configuration (Fig. 3b) was performed and data were fitted with the model. The 22 cm × 22 cm electrode stack (Fig. 3b) was used to determine the power density and energy efficiency at different current densities fixing the residence time at 22 s (flow velocity of 1.0 cm·s$^{-1}$). This was done by increasing the current density in 6.2 A·m$^{-2}$ steps (0.3 A in current over 22 cm × 22 cm area) for 10 min each, taking the average of the last 2 min of the current and voltage values as measured with the potentiostat (IVIUM.XRi, IVIUM Technologies BV, the Netherlands) to obtain the power (Eq. (11)). The blank resistance was measured to be 0.071 Ω, given by REDstack [39], which

comprised the resistance of the electrodes, the rinse solution and the three extra CEMs. This was used to discard the contribution of the electrodes to the stack resistance, which would be negligible when using hundreds of cell pairs. To validate the model, experimental power data were corrected for the blank resistance [39], to avoid the presence of the blank resistance (Eq. (2)) as an additional fitting parameter. Pumping losses across the stack were determined experimentally, and the model parameter $K$ (Eqs. (16) and (17)) was adjusted to fit the experimental data. The shadow factor $f$ was adjusted to fit the experimental data, starting with 0.55, corresponding to the open area of the spacer netting.

### 2.4.2. The relation between electrode segments

To understand the mutual response of the electrode segments, the relation between electrode segments (Fig. 3d) was established by measuring the potential of each segment with a multi-channel potentiostat (IVIUM n-stat, IVIUM Technologies BV, the Netherlands) at a fixed residence time of 22 s (flow velocity of 1.0 cm·s$^{-1}$). This consisted in operating one electrode segment, first at open-circuit voltage (OCV) conditions for 60 s followed by a stepwise increase in the extracted current with 16.5 A·m$^{-2}$ current density steps (0.2 A in current over 11 cm × 11 cm area), for 120 s each, until the stack voltage crossed 0 V. Simultaneously, the OCV of the other three electrode segments was measured continuously. Segment current densities were calculated by dividing the applied current (in A) by one-fourth of the active membrane area.

### 2.4.3. Comparison between single and segmented electrode configurations

The performance of four-electrode segments electrically connected to a single load (referred to as single electrode configuration, Fig. 3c) was compared to the independent performance of the four electrode segments (referred to as segmented electrode configuration, Fig. 3d) and characterized at five different residence times: 88, 44, 22, 15, and 11 s (corresponding to flow velocities of 0.25, 0.50, 1.00, 1.50 and 2.00 cm·s$^{-1}$, respectively). This approach was chosen since connecting the four electrode segments as a single electrode does not change the total electrode area nor the electrode rinse solution distribution, thus providing a fair comparison. In this third experiment, electrochemical measurements were done using sliding rheostats (4.5 Ω 9 A, Eisco, USA) as a variable external load. Each rheostat was connected to a multimeter (Digital Multimeter VC165, Voltcraft, Germany) monitoring the external load voltage. The segment voltage was measured at the electrodes (Fig. S3), while the current was measured using a calibrated shunt of 0.1 Ω. The power per segment was calculated from the measured shunt voltage for each segment and the measured segment voltage (Eq. (11)). The overall power was calculated by summing all segments powers (P1 + P2 + P3 + P4). The experimental power of each electrode segment was monitored automatically inside the data logger as well as the total power. For the single electrode, the maximum power was determined by sliding the rheostat until the peak in the power curve was reached. For the segmented electrode, the individual rheostats were adjusted manually until the overall power value reached its maximum.

The stack power density was obtained by dividing the power by the total active membrane area. The power density per segment was obtained by dividing the segment power by a quarter of the total active membrane area.

## 3. Results and discussion

### 3.1. Model calibration

Fig. 4 shows that the calibrated model correctly predicts the power density and energy efficiency for different external loads. The determined model values of the spacer shadow factor (0.61) and salt diffusion coefficient (6.5 × 10$^{-12}$ m$^2$·s$^{-1}$) are in line with the values

reported by Veerman et al. [21] and in the normal range for ion exchange membranes [40].

### 3.2. The relation between electrode segments

Experimentally obtained I-V curves for each case of one active electrode segment are shown in Fig. 5 for a residence time of 22 s. The first 60 s period, at OCV conditions, shows a different OCV value for each electrode segment depending on their position. Segment 1 (S1) has the highest potential (1.548 V) because the gradient is the largest in this area. This segment receives fresh seawater and river water, i.e. it is the first contact between both solutions and the first opportunity for ion exchange. And it is then followed by S2 (1.543 V), S3 (1.522 V) and S4 (1.514 V). At this stage, the stack is in stationary condition and no current is extracted, thus, the decrease in potential across the stack indicates undesired water and salt diffusion through the membranes, which is expected when using ion-exchange membranes [19]. This is confirmed by the change in concentration between the inlet and outlet of the river and seawater measured at OCV (Fig. S4a). The same behaviour was detected in further experiments at different residence times (Table S2). The decrease in potential across the electrode segments is more evident at longer residence times since the feedwaters have extended contact periods with the membranes. For a single electrode, these phenomena would only be detected through a change in concentration at the final outlets and a difference between the theoretically calculated and the experimentally measured membrane potential. The segmented electrode configuration allows visualization of the effect of undesired salt and water transport. Moreover, it is visible that the potential of each electrode segment is dependent on its position in the stack.

Fig. 5 shows how the electrode segments influence each other when active. When current is extracted from S1 (Fig. 5c), the OCV of S3 drops. This is caused by the increase in salinity of the river water, which flows from S1 to S3. The potential of S2 exhibits a small decrease compared to the drop in OCV of S3, showing that the salinity drop of the seawater has a smaller influence on the OCV of the adjacent segment rather than the increase in salinity of the river water, following the Nernst equation. Additionally, it is worth noting that the potential of S4 is minimally affected. This shows that the feedwaters and the ions follow a straight flow path inside the stack (Fig. 3a). Similarly, when S2 generates current (Fig. 5a), the potential of S4 drops due to the increased salinity of the river water. OCV values of S1 and S3 are not
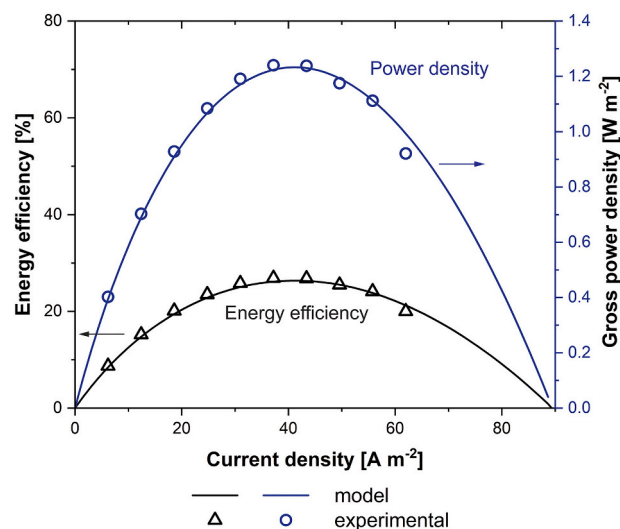


**Fig. 4.** Experimental and modelled gross power density and energy efficiency values for a 22 cm × 22 cm cross-flow stack with 155 μm thick spacers at a residence time of 22 s (flow velocity of 1.0 cm·s$^{-1}$).
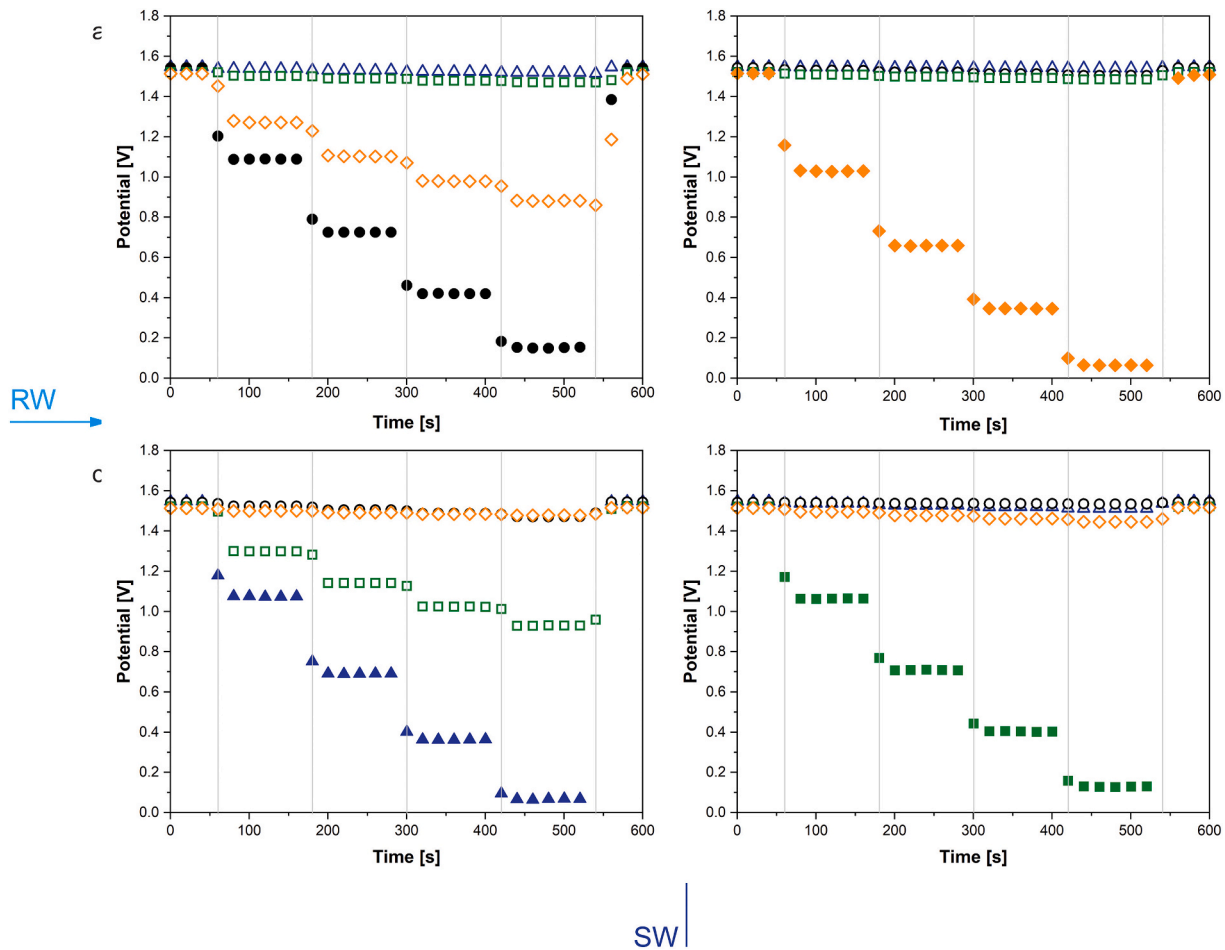
**Fig. 5.** Relation between electrode segments at a residence time of 22 s (1.0 cm·s$^{-1}$ flow velocity). Current density steps of 16.5 A·m$^{-2}$ (0.2 A current divided by 11 cm × 11 cm area) were extracted from one segment (solid marker, also indicated in the plot) and the segment voltage response was measured. In the same time frame, remaining segments (open markers) were measured at OCV conditions. Each plot corresponds to one active electrode segment a) S2 b) S4 c) S1 d) S3, the order was chosen to mimic the position of the segments concerning the RW and SW flow path inside the stack (indicated in the bottom and left by arrows).

affected, providing a further indication that a straight flow path is present inside the stack. When S3 is active (Fig. 5d), only S4 has a shallow drop in potential, supporting the conclusion that the salinity drop in the seawater is not crucial for the driving force. Finally, when S4 is generating current (Fig. 5b), as expected, the OCV values of the other segments are not influenced, indicating that the segments do not communicate with each other, i.e. the electrical field is only working in the electrode segment area. These results indicate that the increase in salinity of the river water mainly determines changes in the electromotive force over the active area [28] and that the electric fields introduced by the electrode segments stay separate through the stack when using a limited number of only 10 cell pairs.

*3.3. Power density distribution model in a single electrode and segmented electrode*

The current density inside the RED stack has a non-homogeneous distribution, as the local currents are a function of 3 parameters: 1) the electromotive force, 2) the internal resistance and 3) the external load. The first two parameters are determined by the local salinity gradient and local concentrations, respectively. This directly affects the local power density output [22,41]. Experimentally this phenomenon can be measured but it is limited to the number of electrode segments available. With a modelling approach, it can be simulated and mapped. For co-flow and counter-flow configurations, the decrease of electromotive force along the flow direction has been shown in several studies

[21,24,26,41]. For cross-flow configuration, Vermaas et al. displayed the current density distribution in the active area, albeit for a RED system with ideal membranes [22].

Fig. 6 compares the gross power density distribution on the active membrane area inside the stack for single electrode configuration (Fig. 6a), segmented electrode configuration at maximized power per segment (Fig. 6b), i.e. when the load is sequentially optimized to maximize the power produced by the individual segments (in the order S1, S2, S3, and S4 due to the flow of the feedwaters from one segment to the next), and segmented electrode configuration at maximized overall power (Fig. 6c), i.e. when the sum of the electrode segments power is maximum. Furthermore, it compares the gross power density contribution (Fig. 6d) per equivalent segment in the single electrode configuration or per independent segment (segmented electrode configuration). The residence time of 44 s was chosen since the electrode segmentation effect is pronounced at longer residence times. In addition to Fig. 6, Fig. S5 illustrates the distribution of the sodium chloride concentration in the river and seawater, the electromotive force, the cell pair resistance, and the current density.

For the single electrode configuration (Fig. 6a), the electrode segments are electrically connected, and the current is controlled by a single external load (Fig. 2c). The gross power density value decreases alongside the river water direction (x-axis) since the electromotive force decreases the most with the increase in salinity of the river water (Fig. S5g), which also results in lower electrical resistance (Fig. S5j). The outcome is different local current densities while the same external
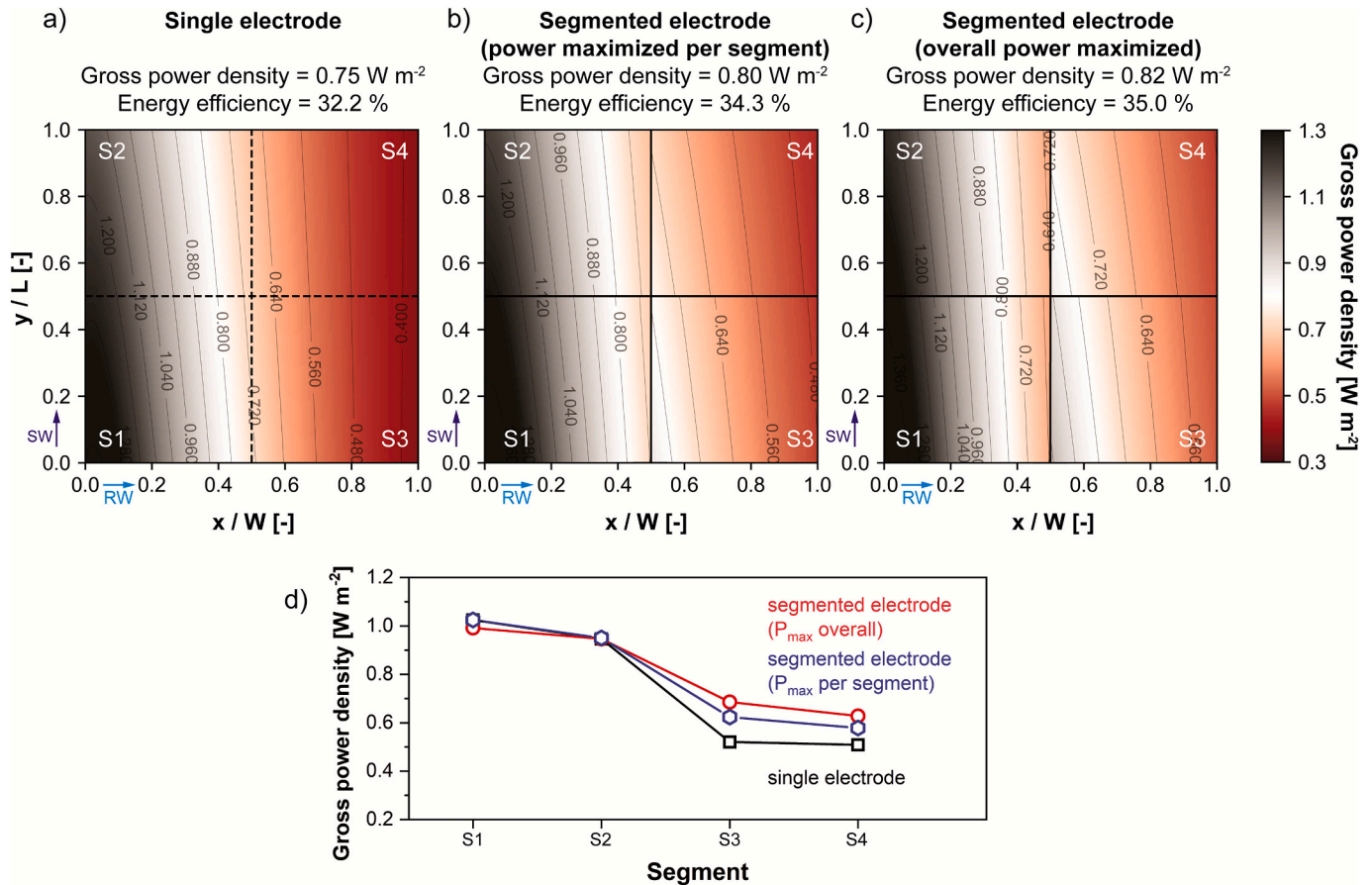
**Fig. 6.** Model results for gross power density distribution inside a 22 cm × 22 cm RED stack in a) the single electrode configuration, b) the segmented electrode configuration at maximized power per segment, and c) the segmented electrode configuration at overall maximum power at a residence time of 44 s (flow velocity of 0.5 cm·s$^{-1}$). The x-axis is the river water path and the y-axis the seawater path. Note, the grid division in a) is only used to allow an easier comparison with b) and c), as in the single electrode configuration the electrode segments electrically work as one. d) Gross power density contribution per equivalent electrode segment (single electrode) and per electrode segment (segmented electrode at maximized power per individual segment and overall maximum power).

load is applied to the stack (Fig. S5m). The highest gross power density is obtained close to the point where the feedwaters first meet, where the electromotive force is still high, but the electrical resistance of the river water is decreasing due to the rising salt concentration. It can be noted that the current distribution (Fig. S5m) and the one Vermaas et al. [22] reported are different. This is due to the membrane electrical resistances, they were assumed zero by Vermaas et al., but are considered in the present work. Fig. 6b and c show the power distribution using a segmented electrode configuration, with four independent external loads (Fig. 2d). Again, the gross power density value decreases along the river water due to mixing. However, by adjusting each external load to the internal segment resistance (Fig. S6), the harvested gross power density is higher compared to the single electrode configuration. Fig. S5g–i shows the difference between the electromotive force and the
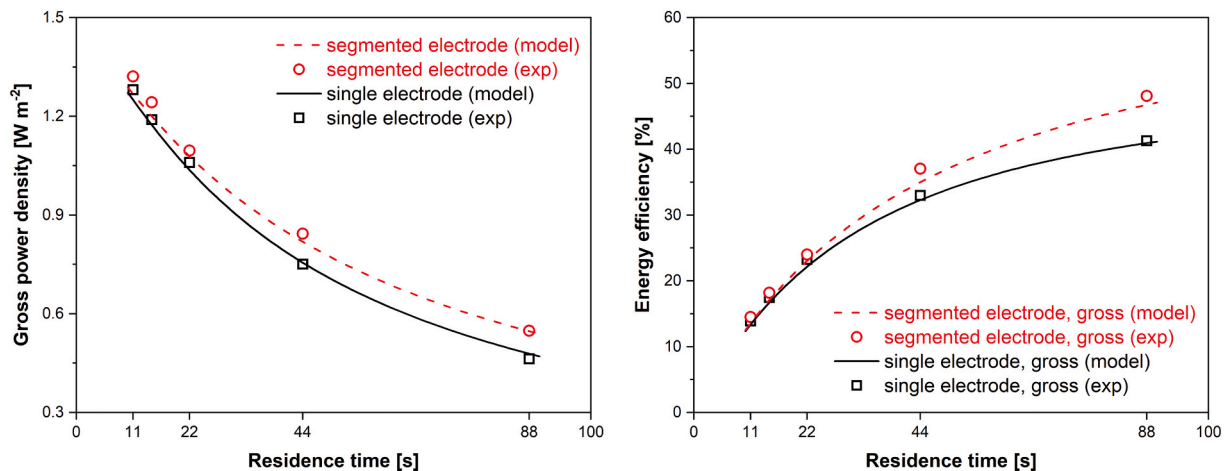


**Fig. 7.** a) Gross power density and b) energy efficiency, for single electrode and segmented electrode configurations, as a function of residence time; symbols represent the experimental data (residence time of 11, 15, 22, 44 and 88 s) and the lines represent the model results. Model parameters can be found in Table S1.

external loads (E-U in Eq. (4)), which together with the local stack resistance contributes to determining the local current density. In Fig. 6d segments S3 and S4 produce a higher gross power density for both segmented electrode configurations. When adjusting the different loads to reach the overall maximum power density, S1 is under-performing the equivalent segment in the single electrode configuration. This is because to reach the overall maximum power density, it is beneficial that S1 does not work at its maximum power density, as in Fig. 6b, but preserve part of the salinity gradient for the following electrode segments, thus allowing higher electromotive force in S3 and S4. It may seem counter-intuitive that segments S3 and S4 produce more power when the overall power is maximized rather than when the power per segment is maximized. When the power per segment is maximized the high performance of S1 and S2 comes at the expense of S3 and S4, which experience a lower salinity gradient. At 44 s residence time, the model predicts a 9% increase in gross power density from a single electrode configuration to the segmented electrode configuration at overall maximum power density. This increase is mainly gained in S3 and S4 (these segments increase power by 24% and 19%, respectively). Furthermore, for optimization, it is important to note that the electrode segments work towards the overall maximum power instead of being maximized segment individually.

### 3.4. The behaviour of a single electrode and a segmented electrode with residence time

In addition to the model results, Fig. 7 presents a comparison of the experimental and model overall stack gross power densities (Fig. 7a) and energy efficiencies (Fig. 7b) for the single electrode and segmented electrode configurations at different residence times when the overall stack power is maximized. In all cases, the model predictions closely resemble the experimental results.

Fig. 7a shows that the gross power density decreases for increasing residence time. This is consistent with the results from the literature [16,19,28]. The opposite trend is observed in Fig. 7b, where energy efficiency increases for longer residence times. These trends have been explained by Moreno et al. as the consequence of lower Gibbs free energy per unit time available at longer residence times, in addition to the non-homogenous distribution of electromotive force, cell resistance, and current density in the active membrane area [19]. Additionally, at longer residence times more ion exchange occurs, which results in a lower electromotive force and stack resistance for the segments further away from the water inlets. At longer residence times, for the single electrode configuration, in the region close to the outlets, the locally available electromotive force becomes close to the external voltage load ($E \sim U$), which leads to small current production (Eq. (4)), hence only a small power output comes from this region. When the single electrode and the segmented electrode configuration are compared, the adaptation of the external loads to the local electromotive force and local stack resistance (i.e. a lower external load on segments S3 and S4), allows to produce a higher current and therefore a higher power output close to the outlets of the stack. If this is combined with the strategy of saving gradient in the first segments (S1 and S2) to reach the overall maximum power, it explains the higher power production for the segmented electrode configuration compared to the single electrode configuration at all residence times, with a pronounced gain at 44 and 88 s.

### 3.5. Electrode segments contribution at different residence times

Data in Fig. 7 provide the overall stack output, based on the contribution of each electrode segment. The contribution of each electrode is shown in Fig. 8, providing the voltage load and gross power density for each electrode segment in the segmented electrode configuration at different residence times, when the maximum overall power is achieved.

In Fig. 8a, for all residence times, the external load voltages on S1

and S2 are similar despite the different extent of ion exchange occurring at different residence times. This indicates that to maximize the overall power segments S1 and S2 work at a sub-optimal point to save gradient for segments S3 and S4. When the feedwaters reach segments S3 and S4, major ion exchange has occurred and the salinity gradient has significantly decreased, with the highest decrease in S4. Since the salinity gradient is considerably lowered in S3 and S4, the external loads need to be adjusted accordingly. Fig. 8a shows that for increasing residence times, the external load voltages for S3 and S4 are decreasing. To achieve maximum power output on these electrode segments, the required external load voltage is lower than for S1 and S2. It can be noted in Fig. S7 that the predicted load voltages, with the model, at maximum power density in the segmented electrode configuration closely resembles the experimentally identified set of values. This agreement between model and experiment highlights the value of the model in guiding the optimization of the external loads. In Fig. 8b, the gross power density per electrode segment is presented. At short residence times, the power output of the four segments is very similar, but with increasing residence times and consequently increased ion exchange, the power density produced by the electrode segments located further away from the river water inlet (S3 and S4) decreases. Interestingly, at short residence times, the load voltages required to produce similar power densities are lower for S3 and S4 than for S1 and S2. This is the case because S1 and S2 operate with a higher electromotive force, but also higher stack resistance. S3 and S4 have a lower electromotive force available but benefit from the increased conductivity of the river water, leading to lower stack electrical resistance and comparable gross power density for all segments.

Fig. 8a shows that the optimal load voltages for S1 and S2 are similar, and the same applies to S3 and S4. The large difference in an optimal external load along the river water and small difference along the seawater flow direction indicates that segmentation along the river water is more beneficial than along the seawater. This is the case because the electromotive force is most sensitive to the salinity of the river water (Fig. S5g and i).

To investigate this hypothesis in further detail, Fig. 9 presents the model results of a 2 × 2 electrode segmentation (Fig. 3d) and a 2 × 1 configuration (along the river flow direction only).
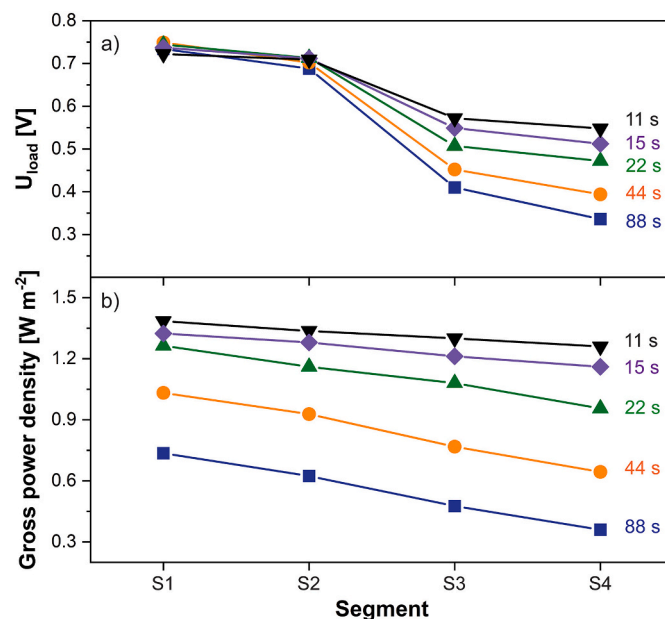


**Fig. 8.** Individual segment contribution (experimental) at different residence times (11, 15, 22, 44, and 88 s) when the overall stack power is maximized. a) The voltage drops over the external load voltage per segment. b) Gross power density per electrode segment.
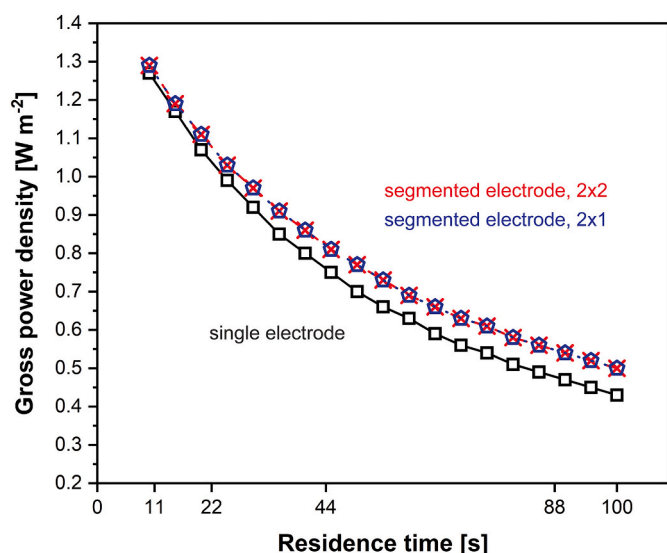
**Fig. 9.** Modelled gross power density as a function of the residence time for a single electrode, two electrode segments (2 × 1, in the river water flow direction), and four-electrode segments (2 × 2) in a 22 cm × 22 cm stack.

The results are nearly identical, with only very small differences at high residence times, between the segmented electrode configurations. This confirms that a simpler configuration with electrode segmentation only along the river water direction, as proposed by Vermaas et al. [22], would yield the same power increase as segmentation along both river and sea directions. Nevertheless, the additional complexity of a 2 × 2 configuration allows for the operational flexibility required by feedwater switch strategies, i.e. changing seawater for river water and vice versa, which have been proved to be beneficial for fouling management [42].

### 3.6. Net power density and net energy efficiency

Fig. 10a shows the pumping power density, which significantly decreases with increasing residence time as longer residence times imply lower feed flow velocities. At short residence times, the pumping power densities are increasing rapidly due to the increase in pressure drop inside the stack [16]. Meanwhile, at long residence times, a flat region is reached where the pumping losses become negligible, being the ideal working region to avoid pumping losses.
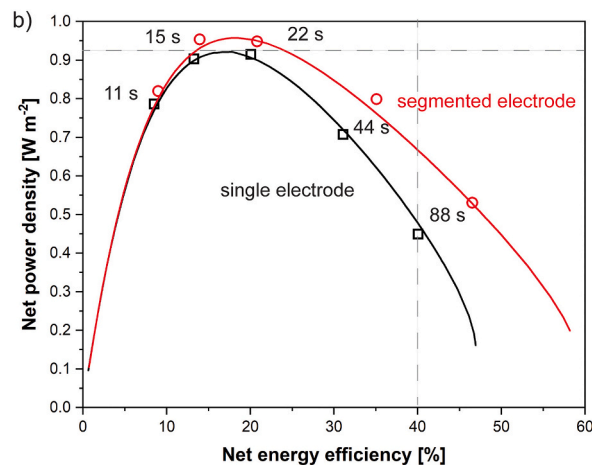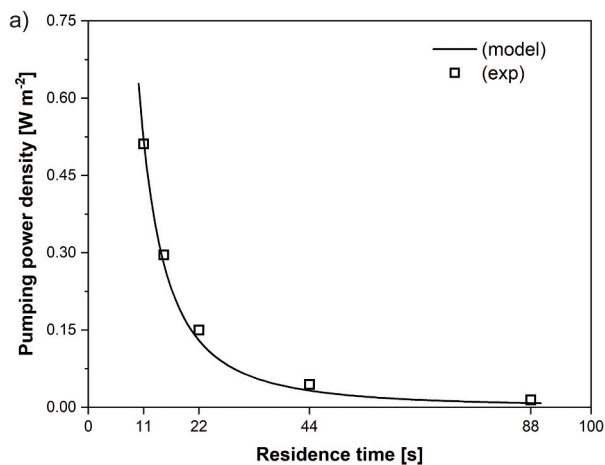
Fig. 10b shows the net power density, i.e. the gross power density minus the pumping power density, plotted against the net energy efficiency. Electrode segmentation leads to higher net power density and efficiency at residence times longer than 11 s. This is the case due to the maximized overall power production. The increased ion exchange for the segmented electrode is evident in the decreased gradient at the stack outlet in Fig. S4b.

The greatest benefit of applying electrode segmentation is reported in Fig. 10b. Both configurations achieve maximum net power density at approximately 17% net energy efficiency and short residence times. This relatively low net energy efficiency is not beneficial for up-scaling RED when the cost of water pre-treatment to decrease fouling is a relevant fraction of the operating costs. To minimize this cost, the energy efficiency should be as high as possible without sacrificing power density. Fig. 10b shows that electrode segmentation accomplishes this requirement. Comparing both electrode configurations at the net power density at the peak performance for a single electrode (0.92 W·m$^{-2}$), segmentation increases the net energy efficiency from 17% for the single electrode to 25% for the segmented electrode (horizontal line in Fig. 10b), which is a remarkable 43% relative efficiency increase. This increase in efficiency allows the extraction of the same power from less water, which is likely to reduce the operating costs of a full-scale RED power plant by reducing the need for water pre-treatment. At 40% net energy efficiency (vertical line in Fig. 10b) the net power output for the segmented electrode configuration is enhanced by 39% relative to a single electrode, which is likely to translate in a lower capital cost for a full-scale plant, as a smaller membrane area is required to achieve a given power production target. Although promising, testing in a larger scale RED system, i.e. more cell pairs, fed with natural feedwaters is necessary to confirm the benefits of electrode segmentation on capital and operating costs. For a segmented electrode, the same net energy efficiency can be reached at a shorter residence time. As the process is more efficient, higher net power densities can be achieved. Therefore, the increase in net power density for a segmented electrode results from combining the increase in power due to shorter residence time (more Gibbs free energy available per unit time) and the increased energy extraction enabled by electrode segmentation. This is especially true in the long residence time region (20–90 s), due to the tuning of the external loads allowing additional power production in S3 and S4. Electrode segmentation thus reduces the trade-off between energy efficiency and power density generation, which is a critical element of the RED process to be considered for large scale RED plants.



**Fig. 10.** a) Pumping power density as a function of residence time. b) Net power density as a function of net energy efficiency for the single electrode and segmented electrode configurations at different residence times. Symbols represent experimental data (residence time of 11, 15, 22, 44 and 88 s) and lines show the model results.

## 4. Conclusions

The present work shows with a validated RED model and experimental investigation that electrode segmentation potentially reduces operating cost or capital expenditure. Operating cost likely decreases by increasing net energy efficiency at a given net power density (43% relative increase in efficiency), which is beneficial in case of high water pre-treatment costs to control fouling. Capital expenditure likely lowers at high net energy efficiencies by increasing the net power density with electrode segmentation decreasing the membrane area needed. The highest gain is attained when optimizing the external loads for overall maximum power, rather than sequentially maximizing the power output of individual segments. At 40% net energy efficiency, the net power output for a segmented electrode is 39% higher ($0.67 \, \mathrm{W \cdot m^{-2}}$) than a single electrode ($0.47 \, \mathrm{W \cdot m^{-2}}$). This increase in net power density at equal net energy efficiency results from combining the increase in power due to shorter residence time and the increased ion exchange enabled by electrode segmentation. This is especially true in the long residence time region (20–90 s), due to the tuning of the external ohmic loads allowing additional power production in the segments adjacent to the river water outlet. These experiments were conducted at a laboratory scale with 10 cell pairs. The effect of electrode segmentation in a larger membrane pile needs therefore further study. Experiments and the model confirm that segmenting along the river water direction in a cross-flow stack gives the most benefit, indicating that segmentation can be simplified to two rectangular electrode segments when switching the feedwaters is not required.

## Author statement

Catarina Simões and Diego Pintossi: Conceptualization, Investigation, Methodology, Validation, Visualization, Writing – Original draft.

Michel Saakes, Zandrie Borneman, Wim Brilman, Kitty Nijmeijer: Conceptualization, Funding acquisition, Methodology, Resources, Supervision, Writing – Review and Editing.

## Declaration of competing interest

The authors declare that they have no known competing financial interests or personal relationships that could have appeared to influence the work reported in this paper.

## Acknowledgements

## Appendix A. Supplementary data

Supplementary data to this article can be found online at https://doi.org/10.1016/j.desal.2020.114604.

## References

[1] U.N.F. Convention on Climate Change, Paris Agreement, https://unfccc.int/files/essential_background/convention/application/pdf/english_paris_agreement.pdf, (2015), Accessed date: 21 January 2020.

[2] W.J. Van Egmond, M. Saakes, S. Porada, T. Meuwissen, C.J.N. Buisman, H.V.M. Hamelers, The concentration gradient flow battery as electricity storage system: technology potential and energy dissipation, J. Power Sources (2016), https://doi.org/10.1016/j.jpowsour.2016.05.130.

[3] J. Veerman, M. Saakes, S.J. Metz, G.J. Harmsen, Reverse electrodialysis: performance of a stack with 50 cells on the mixing of sea and river water, J. Memb. Sci. (2009), https://doi.org/10.1016/j.memsci.2008.11.015.

[4] J. Kuleszo, C. Kroeze, J. Post, B.M. Fekete, The potential of blue energy for reducing emissions of CO2 and non-CO2 greenhouse gases, J. Integr. Environ. Sci. (2010), https://doi.org/10.1080/19438151003680850.

[5] R.E. Pattle, Production of electric power by mixing fresh and salt water in the hydroelectric pile, Nature (1954), https://doi.org/10.1038/174660a0.

[6] R.E. Lacey, Energy by reverse electrodialysis, Ocean Eng. 7 (2005) 1–47, https://doi.org/10.1016/0029-8018(80)90030-x.

[7] E. Güler, W. van Baak, M. Saakes, K. Nijmeijer, Monovalent-ion-selective membranes for reverse electrodialysis, J. Memb. Sci. (2014), https://doi.org/10.1016/j.memsci.2013.12.054.

[8] H. Gao, B. Zhang, X. Tong, Y. Chen, Monovalent-anion selective and antifouling polyelectrolytes multilayer anion exchange membrane for reverse electrodialysis, J. Memb. Sci. (2018), https://doi.org/10.1016/j.memsci.2018.09.035.

[9] X.L. Wang, M. Wang, Y.X. Jia, B.B. Wang, Surface modification of anion exchange membrane by covalent grafting for imparting permselectivity between specific anions, Electrochim. Acta (2015), https://doi.org/10.1016/j.electacta.2015.06.115.

[10] D.A. Vermaas, M. Saakes, K. Nijmeijer, Power generation using profiled membranes in reverse electrodialysis, J. Memb. Sci. (2011), https://doi.org/10.1016/j.memsci.2011.09.043.

[11] D.A. Vermaas, M. Saakes, K. Nijmeijer, Early detection of preferential channeling in reverse electrodialysis, Electrochim. Acta (2014), https://doi.org/10.1016/j.electacta.2013.11.094.

[12] Z. He, X. Gao, Y. Zhang, Y. Wang, J. Wang, Revised spacer design to improve hydrodynamics and anti-fouling behavior in reverse electrodialysis processes, Desalin. Water Treat. (2016), https://doi.org/10.1080/19443994.2016.1186569.

[13] J. Moreno, N. de Hart, M. Saakes, K. Nijmeijer, CO 2 saturated water as two-phase flow for fouling control in reverse electrodialysis, Water Res. (2017), https://doi.org/10.1016/j.watres.2017.08.015.

[14] E.J. Bodner, M. Saakes, T. Sleutels, C.J.N. Buisman, H.V.M. Hamelers, The RED fouling monitor: a novel tool for fouling analysis, J. Memb. Sci. (2019), https://doi.org/10.1016/j.memsci.2018.10.059.

[15] D. Pintossi, M. Saakes, Z. Borneman, K. Nijmeijer, Electrochemical impedance spectroscopy of a reverse electrodialysis stack: a new approach to monitoring fouling and cleaning, J. Power Sources 444 (2019) 227302, https://doi.org/10.1016/j.jpowsour.2019.227302.

[16] D.A. Vermaas, M. Saakes, K. Nijmeijer, Doubled power density from salinity gradients at reduced intermembrane distance, Environ. Sci. Technol. (2011), https://doi.org/10.1021/es2012758.

[17] S. Pawlowski, T. Rijnaarts, M. Saakes, K. Nijmeijer, J.G. Crespo, S. Velizarov, Improved fluid mixing and power density in reverse electrodialysis stacks with chevron-profiled membranes, J. Memb. Sci. (2017), https://doi.org/10.1016/j.memsci.2017.03.003.

[18] I. Choi, J.Y. Han, S.J. Yoo, D. Henkensmeier, J.Y. Kim, S.Y. Lee, J. Han, S.W. Nam, H.J. Kim, J.H. Jang, Experimental investigation of operating parameters in power generation by lab-scale reverse electro-dialysis (RED), Bull. Kor. Chem. Soc. (2016), https://doi.org/10.1002/bkcs.10810.

[19] J. Moreno, S. Grasman, R. van Engelen, K. Nijmeijer, Up-scaling reverse electrodialysis, Environ. Sci. Technol. (2018), https://doi.org/10.1021/acs.est.8b01886.

[20] J. Veerman, J.W. Post, M. Saakes, S.J. Metz, G.J. Harmsen, Reducing power losses caused by ionic shortcut currents in reverse electrodialysis stacks by a validated model, J. Memb. Sci. (2008), https://doi.org/10.1016/j.memsci.2007.11.032.

[21] J. Veerman, M. Saakes, S.J. Metz, G.J. Harmsen, Reverse electrodialysis: a validated process model for design and optimization, Chem. Eng. J. 166 (2011) 256–268, https://doi.org/10.1016/j.cej.2010.10.071.

[22] D.A. Vermaas, J. Veerman, N.Y. Yip, M. Elimelech, M. Saakes, K. Nijmeijer, High efficiency in energy generation from salinity gradients with reverse electrodialysis, ACS Sustain. Chem. Eng. (2013), https://doi.org/10.1021/sc400150w.

[23] M. Ciofalo, M. La Cerva, M. Di Liberto, L. Gurreri, A. Cipollina, G. Micale, Optimization of net power density in reverse electrodialysis, Energy. 181 (2019) 576–588, https://doi.org/10.1016/j.energy.2019.05.183.

[24] M. Tedesco, A. Cipollina, A. Tamburini, W. van Baak, G. Micale, Modelling the reverse electrodialysis process with seawater and concentrated brines, Desalin. Water Treat. 49 (2012) 404–424, https://doi.org/10.1080/19443994.2012.699355.

[25] J.W. Post, C.H. Goeting, J. Valk, S. Goinga, J. Veerman, H.V.M. Hamelers, P.J.F.M. Hack, Towards implementation of reverse electrodialysis for power generation from salinity gradients, Desalin. Water Treat. 16 (2010) 182–193, https://doi.org/10.5004/dwt.2010.1093.

[26] M. Tedesco, A. Cipollina, A. Tamburini, G. Micale, Towards 1 kW power production in a reverse electrodialysis pilot plant with saline waters and concentrated brines, J. Memb. Sci. 522 (2017) 226–236, https://doi.org/10.1016/j.memsci.2016.09.015.

[27] A. Daniilidis, R. Herber, D.A. Vermaas, Upscale potential and financial feasibility of a reverse electrodialysis power plant, Appl. Energy (2014), https://doi.org/10.1016/j.apenergy.2013.12.066.

[28] J. Veerman, M. Saakes, S.J. Metz, G.J. Harmsen, Electrical power from sea and river water by reverse electrodialysis: a first step from the laboratory to a real power plant, Environ. Sci. Technol. (2010), https://doi.org/10.1021/es1009345.

[29] D.A. Vermaas, D. Kunteng, M. Saakes, K. Nijmeijer, Fouling in reverse

electrodialysis under natural conditions, Water Res. (2013), https://doi.org/10.1016/j.watres.2012.11.053.

[30] A.M. Weiner, R.K. McGovern, J.H. Lienhard V., A new reverse electrodialysis design strategy which significantly reduces the levelized cost of electricity, J. Memb. Sci. 493 (2015) 605–614, https://doi.org/10.1016/j.memsci.2015.05.058.

[31] M. Geske, M. Heuer, G. Heideck, Z.A. Styczynski, Current density distribution mapping in PEM fuel cells as an instrument for operational measurements, Energies (2010), https://doi.org/10.3390/en3040770.

[32] M. Noponen, T. Mennola, M. Mikkola, T. Hottinen, P. Lund, Measurement of current distribution in a free-breathing PEMFC, J. Power Sources (2002), https://doi.org/10.1016/S0378-7753(01)01063-1.

[33] J.T. Clement, D.S. Aaron, M.M. Mench, In situ localized current distribution measurements in all-vanadium redox flow batteries, J. Electrochem. Soc. (2016), https://doi.org/10.1149/2.0241601jes.

[34] A. Bhattarai, N. Wai, R. Schweiss, A. Whitehead, G.G. Scherer, P.C. Ghimire, T.D. Nguyen, H.H. Hng, Study of flow behavior in all-vanadium redox flow battery using spatially resolved voltage distribution, J. Power Sources (2017), https://doi.org/10.1016/j.jpowsour.2017.06.039.

[35] D. Tvrzník, Effect of electrode area on demineralization performance and the distribution of current density in an industrial-scale electrodialysis stack, Desalination (2017), https://doi.org/10.1016/j.desal.2017.03.002.

[36] G. Doornbusch, H. Swart, M. Tedesco, J. Post, Z. Borneman, K. Nijmeijer, Current utilization in electrodialysis: electrode segmentation as alternative for multistaging, Desalination. 480 (2020) 114243, https://doi.org/10.1016/j.desal.2019.114243.

[37] X. Ge, X. Wang, M. Zhang, S. Seetharaman, Correlation and prediction of activity and osmotic coefficients of aqueous electrolytes at 298.15 K by the modified TCPC model, J. Chem. Eng. Data (2007), https://doi.org/10.1021/je060451k.

[38] J. Moreno, E. Slouwerhof, D.A. Vermaas, M. Saakes, K. Nijmeijer, The breathing cell: cyclic Intermembrane distance variation in reverse electrodialysis, Environ. Sci. Technol. (2016), https://doi.org/10.1021/acs.est.6b02668.

[39] J. Moreno, Private Communication, (2019).

[40] J. Veerman, R.M. de Jong, M. Saakes, S.J. Metz, G.J. Harmsen, Reverse electrodialysis: comparison of six commercial membrane pairs on the thermodynamic efficiency and power density, J. Memb. Sci. (2009), https://doi.org/10.1016/j.memsci.2009.05.047.

[41] M.L. La Cerva, M. Di Liberto, L. Gurreri, A. Tamburini, A. Cipollina, G. Micale, M. Ciofalo, Coupling CFD with a one-dimensional model to predict the performance of reverse electrodialysis stacks, J. Memb. Sci. 541 (2017) 595–610, https://doi.org/10.1016/j.memsci.2017.07.030.

[42] D.A. Vermaas, D. Kunteng, J. Veerman, M. Saakes, K. Nijmeijer, Periodic feedwater reversal and air sparging as antifouling strategies in reverse electrodialysis, Environ. Sci. Technol. (2014), https://doi.org/10.1021/es4045456.